GUNN OR TRANSFERRED-ELECTRON DEVICES

Among all solid-state microwave devices, transferred-electron devices (TEDs), often called Gunn devices, are unique in that they utilize specific bulk-material properties of certain semiconductors. They are unipolar devices and, generally, do not exhibit the distinctive diode characteristic of p–n junctions as seen, for example, in other two-terminal microwave devices, such as impact ionization avalanche transit-time (IMPATT) or tunnel injection transit-time (TUNNETT) diodes (see Transit time devices and Impatt diode and circuits). Originally, TED structures and circuits were developed for both amplifier and oscillator applications. However, rapid progress in high-speed and high-frequency three-terminal devices (see, for example, Heterojunction bipolar transistor and Heterostructure devices) with excellent noise performance is practically eliminating TEDs from all low-noise preamplifier applications up to the high millimeter-wave frequencies. Additionally, oscillators or amplifiers with three-terminal devices continue to reach higher and higher frequencies and offer similar or even higher radio-frequency (RF) output power levels and direct-current (dc)-to-RF conversion efficiencies compared to the most powerful two-terminal devices, such as IMPATT diodes. TEDs in oscillator applications are characterized by low noise and medium RF output power P_{RF}. Therefore, they are well-suited for local oscillators in receivers and transmitters for frequencies above 30 GHz.

PRINCIPLES OF OPERATION

The transferred-electron effect only depends on a specific band structure of the semiconductor material and, therefore, is present in the bulk material. Several materials, mainly in the groups of III–V and II–VI compound semiconductors and listed in Table 1 (1–3), exhibit such a band structure. These semiconductor materials have more than one energy minimum (i.e., valley in the conduction band) and meet the following criteria, which were proposed independently by Ridley and Watkins (4) and by Hilsum (5) (RWH):

1. At least two valleys must be present in the conduction band.
2. The minimum (minima) of the upper valley(s) must be several times the thermal energy of electrons above the minimum of the lowest (= main) valley in the conduction band for electrons to initially reside in the lowest valley.
3. The energy difference (ΔE) between the minimum (minima) of the upper valley(s) and the minimum of the main valley in the conduction band must be less than the energy bandgap E_g to avoid the onset of significant impact ionization in such a device.
4. The transfer of electrons from one conduction band valley to another must require much less time than one period of the intended operation frequency.
5. The effective masses and densities of states in the upper valley(s) must be considerably higher than in the main valley. As a consequence of the higher effective masses, mobilities in the upper valley(s) must be much lower than those in the main valley.

For the principles of operation, a homogeneous bulk semiconductor material and a simplified band structure as shown in Fig. 1 are assumed. Electrons at low energies initially reside in the main valley of the conduction band, where a low effective mass corresponds to a high mobility μ_1. When electrons acquire more energy (e.g., under an electric field $\mathscr{E}$), most of them still remain in the main valley if $\mathscr{E} < \mathscr{E}_{th}$, where $\mathscr{E}_{th}$ is referred to as the threshold electric field. As elec-

Table 1. Semiconductor Materials Related to the Transferred-Electron Effect

Semiconductor	E_g (eV)	Valley Separation Between	Valley Separation ΔE (eV)	$\mathscr{E}_T$ (kV/cm)	v_p (10^7 cm/s)	T (K)
GaAs	1.42	L and Γ	0.31 (0.33)	3.2–3.5	2.2–2.3	300
InP	1.35	L and Γ	0.53 (0.45)	10–12	2.5–2.8	300
Ge	0.74	L and Γ	0.18	2.3	1.4	77
CdTe	1.50	L and Γ	0.51	11.0	1.5	300
InAs	0.36	L and Γ	10.87	12.5	3.6	300
InSb	0.28	L and Γ	0.41	0.6	5.0	77
ZnSe	2.60	L and Γ	—	38.0	1.5	300
$Ga_{0.5}In_{0.5}Sb$	0.36	L and Γ	0.36	0.6	2.5	300
$Ga_{0.3}In_{0.7}Sb$	0.24	L and Γ	—	0.6	2.9	300
$In_{0.53}Ga_{0.47}As$	0.76	L and Γ	0.55	3–4	2.9	300
$InAs_{0.2}P_{0.8}$	1.10	L and Γ	0.95	5.7	2.7	300
$Ga_{0.13}In_{0.87}As_{0.37}P_{0.63}$	1.05	L and Γ	—	5.5–8.6	1.2	300
GaN	3.36	X and Γ	1.5	80–160	2.5–4.5	300
$Ga_{0.5}Al_{0.5}N$	4.77	X and Γ	0.44	>70	2.5	300

Data from Refs. 1 to 3.

trons acquire even more energy (for $\mathscr{E} > \mathscr{E}_{th}$), many of them are scattered ("transferred") into the upper valley, where a higher effective mass corresponds to a lower mobility μ_2 (1). When the electric field is assumed to be constant in the bulk material and n_1 and n_2 denote the number of electrons in the lower and upper valleys, respectively, an average electron velocity $\overline{v}$ and average mobility $\overline{\mu}$ can be defined as

$$\overline{v} = \frac{n_1\mu_1 + n_2\mu_2}{n_1 + n_2}\mathscr{E} = \overline{\mu}\mathscr{E} \tag{1}$$

Since n_1 decreases and n_2 increases, $\overline{v}$ decreases as shown in Fig. 2. At large energies [i.e., high electric fields ($\mathscr{E} \gg \mathscr{E}_{th}$)], most of the electrons are transferred to the upper valley and $n_1 \ll n_2$. Therefore, after reaching the minimum value, the average drift velocity again increases for higher electric fields. The decrease in the average drift velocity for $\mathscr{E} > \mathscr{E}_{th}$ generates a region of negative differential mobility $\overline{\mu}_d$ with

$$\overline{\mu}_d = \frac{d\overline{v}}{d\mathscr{E}} \tag{2}$$

If electrons in the upper valley reach a region where the electric field $\mathscr{E}$ drops below $\mathscr{E}_{th}$, they lose energy and significantly more of them are scattered back to the main valley.

James B. Gunn was the first to observe current oscillations experimentally in bulk GaAs and InP (6,7), which were subsequently explained by this transferred-electron effect (8). As a result, the name Gunn device quickly became common for this type of device. Out of more than ten semiconductor materials known for the transferred-electron effect, only GaAs and InP have so far found widespread use in system applications. GaAs and InP have three valleys in the conduction band, and at the doping concentrations required for operation at millimeter-wave frequencies, high-field mobilities are considerably lower than the low-field mobilities. As a consequence of two upper valleys and additional scattering mechanisms, the electron drift velocity v monotonically decreases for electric fields above $\mathscr{E}_{th}$. Figure 3 shows simplified band structure diagrams for GaAs and InP, and Fig. 4 shows their respective velocity–electric field profiles. Table 2 (9–11) summarizes the relevant material characteristics of GaAs and InP. The finite time it takes for electrons to gain or lose energy in an electric field causes a fundamental physical frequency limit in these devices.

Except for some rare conditions in devices at lower microwave frequencies, the bulk negative differential mobility alone does not cause a static negative differential resistance to be used for RF power generation. A mechanism based on the negative differential mobility results in a dynamic negative resistance as shown next. In a region of bulk semiconductor material under uniform conditions (doping concentration N_D, electric field $\mathscr{E}$, average differential mobility $\overline{\mu}_d$), any space charge inhomogeneity $Q_s(x, t)$ traveling at the velocity v grows or decays following an exponential law that can be derived from Maxwell' s equations:

$$Q_s(x,t) = Q_s(x - vt, 0)\exp\left(-\frac{t}{\tau}\right) \tag{3}$$

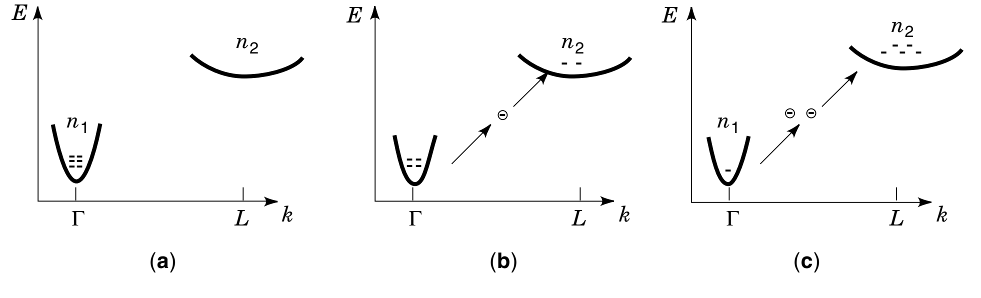

Figure 1. Simplified energy band diagram for a direct two-valley semiconductor showing electron transfer. (a) Electron distribution for $\mathscr{E} < \mathscr{E}_{th}$. (b) Electron distribution for $\mathscr{E} > \mathscr{E}_{th}$. (c) Electron distribution for $\mathscr{E} \gg \mathscr{E}_{th}$.

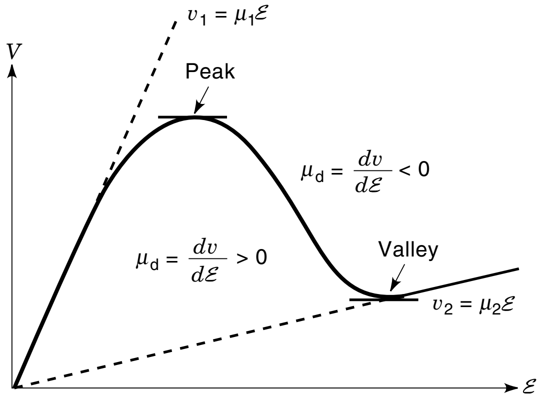

Figure 2. Velocity–electric field profile for the two-valley semiconductor of Fig. 1.

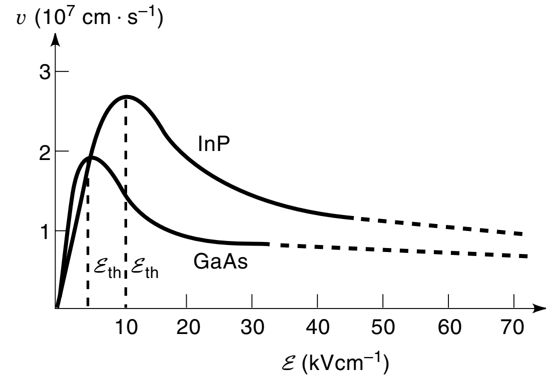

Figure 4. Velocity–electric field profile for the three-valley semiconductor materials GaAs and InP.

where

$$\tau = \frac{\epsilon_s}{\sigma} = \frac{\epsilon_s}{qN_D\overline{\mu}_d} \tag{4}$$

In Eq. (4), q denotes the elementary charge; σ and ϵ_s denote specific conductivity and dielectric constant of the material, respectively. At low electric fields $\mathcal{E}$ where $\overline{\mu}_d > 0$, the charge inhomogeneity decays with $\tau = \tau_D$, the dielectric relaxation time, and at higher electric fields, where $\overline{\mu}_d < 0$, a charge inhomogeneity can grow. This charge inhomogeneity reaches a significant level only if the growth factor for the maximum traveled distance l, the length of the active region of the device, is very large. Therefore, the condition

$$\frac{l}{v|\tau|} = \frac{lqN_D|\overline{\mu}_d|}{\epsilon_s v} > 1 \tag{5}$$

must be satisfied, which corresponds to

$$N_D l > 1 \times 10^{12}\,\text{cm}^{-2} \tag{6}$$

for both GaAs and InP.

Typical Gunn devices at millimeter-wave frequencies have $N_D l$ products between 1×10^{12} cm^{-2} and 3×10^{12} cm^{-2}, and doping concentrations N_D in the active region exceed 10^{15} cm^{-3}. For $N_D > 10^{15}$ cm^{-3}, space-charge inhomogeneities typically grow into so-called dipole domains where accumulation and depletion layers are lumped together. Figure 5 shows the carrier distribution and electric-field profile for such a dipole domain under uniform conditions. Electrons in the low-field region travel at a constant v_T for a constant electric field $\mathcal{E}_1$. Electrons in region a are accelerated by the higher electric field until they reach region b, where they are transferred to the upper valley and slow down to be trapped in this accumulation region. Electrons in region c lose energy and are trans-

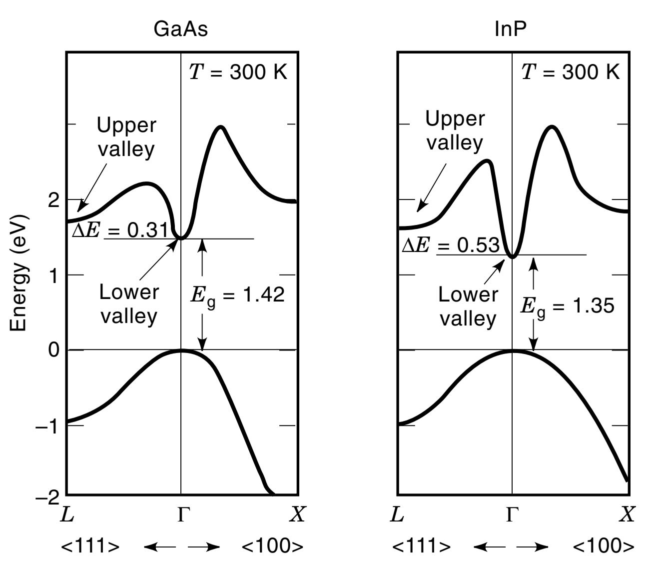

Figure 3. Simplified band diagram for the three-valley semiconductor materials GaAs and InP.

Table 2. Semiconductor Material Characteristics Relevant to GaAs and InP TEDs (at a temperature of 300 K unless noted otherwise)

Properties	Semiconductor	
	GaAs	InP
Energy gap (eV)	1.42	1.34
Low-field mobility (at 500 K) (cm^2 · V^{-1} · s^{-1})	5000	3000
Thermal conductivity (W · cm^{-1} · K^{-1})	0.37–0.54	0.68–0.80
Velocity peak-to-valley ratio	2.2	3.5
Threshold field $\mathcal{E}_{th}$ (kV · cm^{-1})	3.5	10.5
Breakdown field (at $N_D = 10^{16}$ cm^{-3}) (kV · cm^{-1})	400	500
Effective transit velocity v_T (cm · s^{-1})	0.7×10^7	1.2×10^7
Temperature dependence of v_T (K^{-1})	0.0015	0.001
Diffusion coefficient–mobility ratio at 2 $\mathcal{E}_{th}$ (cm^2 · s^{-1})	72	142
Energy relaxation time due to collisions (ps)	0.4–0.6	0.2–0.3
Intervalley relaxation time (ps)	—	0.25
Acceleration–deceleration time (ps) (Inertial energy time constant)	1.5	0.75

After Wandinger (9), Fank et al. (10), and Eddison (11).

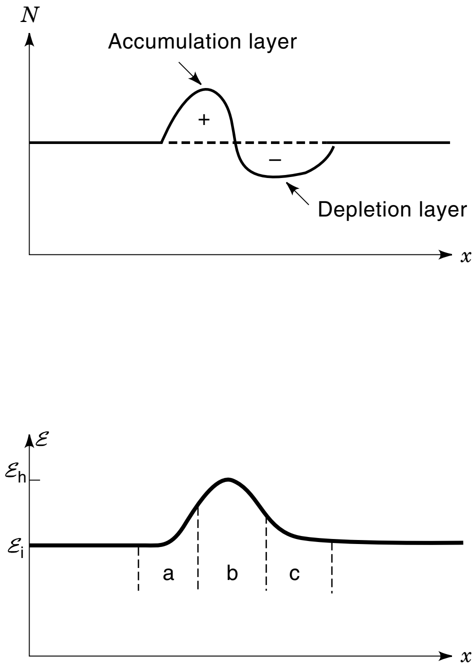

Figure 5. Carrier concentrations and electric field profile for a dipole domain.

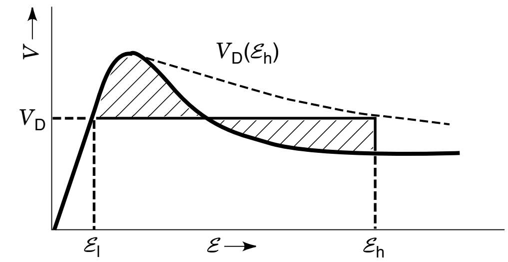

Figure 6. Equal area rule for TEDs.

ferred back to the lower valley. Their average velocity now is higher than the average velocity in region b, thus region c is depleted of electrons. After a domain forms at the cathode, grows, and propagates through the active region, the voltage drop across the domain increases and, under a constant bias voltage, lowers the voltage drop outside the domain. This voltage drop is equivalent to a reduction in the electric field $\mathscr{E}_1$ outside the domain and generally prevents formation of new domains in the active region. It also limits the growth of the existing domain because fewer electrons are trapped in the accumulation layer or escape the depletion layer. Domains reaching the anode collapse and induce a current flow in the external circuit. The phase difference between current and voltage causes a dynamic negative resistance and generates RF power in an appropriate circuit.

Distinctive modes of operation have been investigated and described for TEDs at microwave frequencies (12). However, as is shown next, at millimeter-wave frequencies, finite intervalley transfer and domain-formation times reach a significant fraction of the RF cycle. In such a case, domains form, grow, and suppress formation of new domains, but may never reach the stable state before they reach the anode as described above. Therefore, modes get blurred, and devices generally operate in a near transit-time mode, where the operating frequency f_{op} is given by

$$f_{op} = \frac{v_T}{l} \tag{7}$$

The effective transit velocity $v_T = v(\mathscr{E}_1) = v_D(\mathscr{E}_h)$ can be determined from Butcher's equal-area rule (13), which is

$$\int_{\mathscr{E}_1}^{\mathscr{E}_h} [v(\mathscr{E}) - v_D]\, d\mathscr{E} = 0 \tag{8}$$

for a constant diffusion coefficient throughout the active region and is illustrated in Fig. 6.

If the operating frequency f_{op} differs somewhat from Eq. (7), the domain reaches the anode prematurely or is delayed. Similar to the operation of transit-time diodes, the current pulse from the collapsing domain still causes a negative resistance and generates RF power. Therefore, operation over a broad bandwidth can be achieved. Additionally, higher bias voltages increase electric fields in the device, and higher electric fields reduce the domain velocity v_D, as seen in Fig. 6. At higher electric fields, electrons also acquire the energy for intervalley transfer over a shorter distance, as will be described in more detail later. Consequently, the portion of the active region where domains form and travel is increased.

Figure 7 gives an overview of typical structures and schematic doping profiles for TEDs that have yielded excellent RF performance. The three-zone flat-doping and the two-zone flat-doping structures were the first to be exploited because they are easy to grow in more classical growth systems, such as liquid-phase or vapor-phase epitaxy (LPE or VPE). The three-zone flat-doping structure (14) consists of the n^- doped active region sandwiched between the highly doped n^+ regions for the ohmic contacts. Since low-ohmic alloyed contacts can be formed on n-type GaAs and InP, the highly doped region on the cathode side can be omitted and just a two-zone flat-doping structure needs to be grown by VPE or LPE.

The advent of advanced growth techniques, such as molecular beam epitaxy (MBE), metalorganic chemical vapor depo-

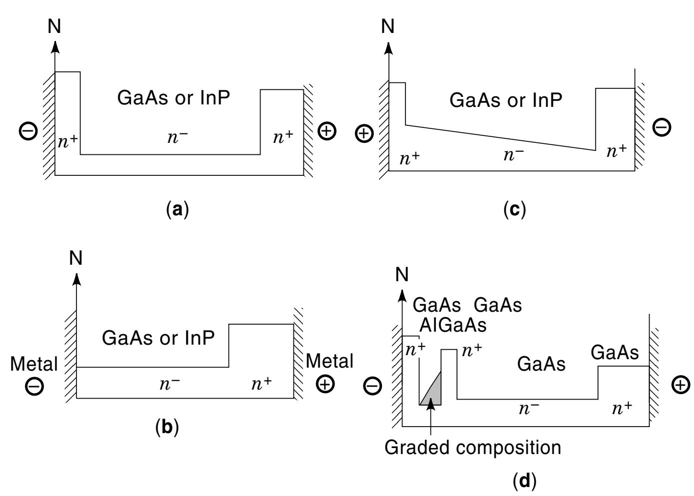

Figure 7. Different device structures for TEDs. (a) Three-zone flat-doping, (b) two-zone flat-doping, (c) three-zone graded doping, and (d) heterojunction-barrier cathode.

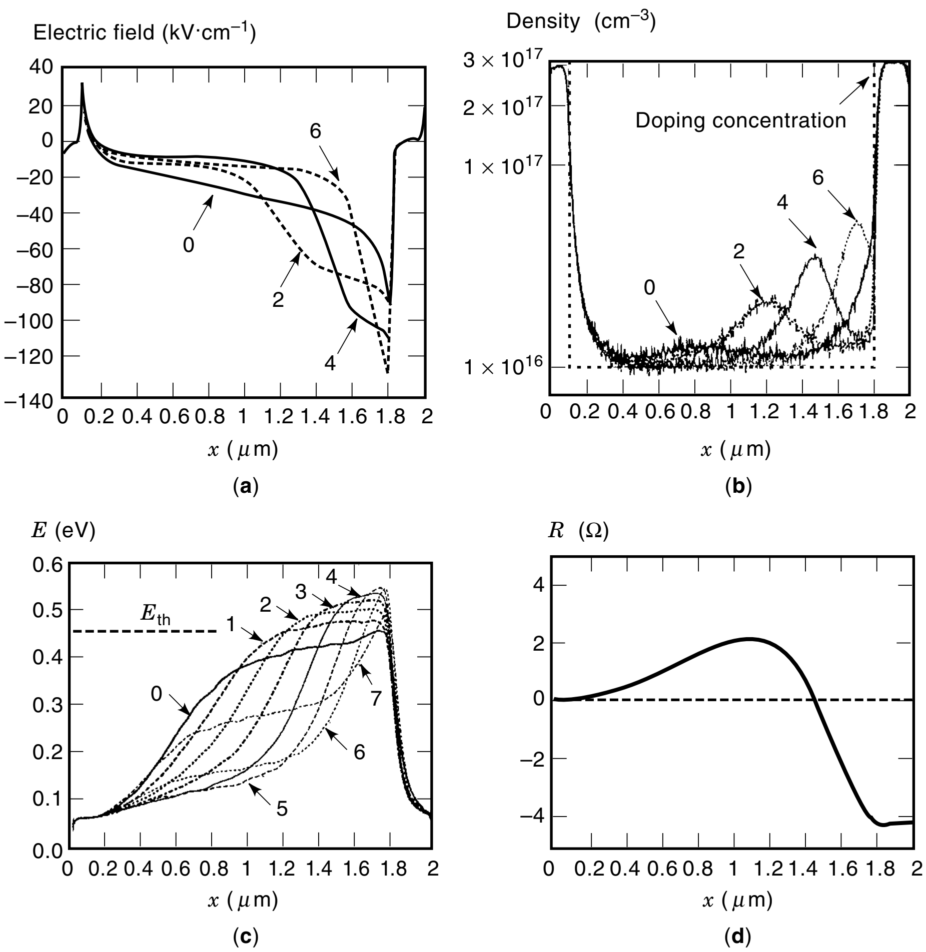

Figure 8. Evolution of (a) electric field, (b) electron density, (c) average electron energy E, and (d) diode resistance R as a function of position x (active region from 0.1 μm to 1.8 μm): f = 95 GHz, V_{rf} = 1.0 V, V_{bias} = 5.0 V, I_{bias} = 474 mA, T = 500 K. The graphs in parts (a), and (b) show the electric field and the electron density, respectively, at $\omega t = n\pi/4$, n = 0, 2, 4, 6, and part (c) shows the electron energy profile at $\omega t = n\pi/4$, n = 0, . . ., 7, during one RF cycle.

sition (MOCVD), metalorganic molecular-beam epitaxy (MOMBE), and chemical-beam epitaxy (CBE) has allowed more complicated structures to be grown. Using these growth techniques, graded doping profiles and heterojunction barriers, as shown in Fig. 7, can be incorporated into the device structures and suitably tailored to optimize device performance at a particular frequency or to extend the frequency limit of TEDs. Computer simulations (11,15,16) have revealed that in a three-zone flat-doping structure, "cold" electrons at low energies entering the active region from the contact zone at the cathode require some time to acquire enough energy to transfer to the upper valley. The results of such Monte Carlo simulations (16) at a frequency of 95 GHz are illustrated in Fig. 8 for a three-zone flat-doping structure in InP with a doping of 1 × 10^{16} cm^{-3} in the active region. The finite energy relaxation times, which are shown in Fig. 9 as a function of the electron energy in GaAs and InP, create a huge so-called dead space at the beginning of the 1.7-μm-long active region. As can be seen from Fig. 8(c), the average energy E of electrons within the dead space does not reach the threshold energy E_{th} for intervalley transfer, and electrons mainly reside in the main valley. Therefore, the differential mobility remains positive, and space-charge inhomogeneities are prevented from growing, which is illustrated in Fig. 8(b) with insignificant electron accumulation within the dead space. As a consequence, the resistance of the device $R(x)$ [i.e., the real part of $\mathbf{Z}(x)$] as a function of the position x,

$$\boldsymbol{Z}(x) = R(x) + jX(x) = \frac{\displaystyle\int_0^x \mathscr{E}(x')\,dx'}{\displaystyle\frac{A}{l}\int_0^x \boldsymbol{J}(x')\,dx'} \tag{9}$$

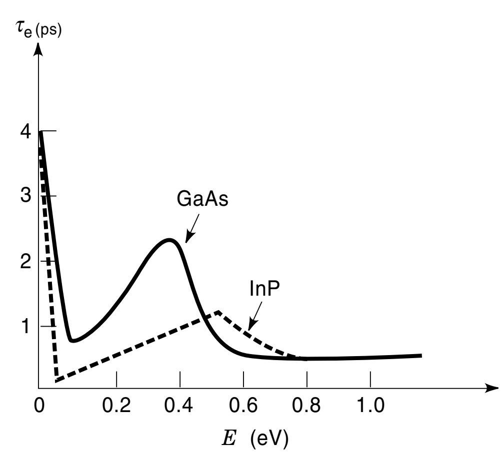

Figure 9. Energy relaxation times τ_e in GaAs and InP as a function of the electron energy E. [After Rolland et al. (15), with permission.]

remains positive for a large fraction of the active region and contributes to losses in this dead-space region, whereas a negative resistance contributes to the RF power generation only for a small fraction of the active region. In Eq. (9), A and $\boldsymbol{J}$ denote the device area and total current density, respectively. In addition to this dead-space region, the peak electric field occurs near the anode, and, at a high dc bias, the electric field may reach values for the onset of avalanche breakdown. The energy-dependent energy relaxation times of Fig. 9 lead to effective transfer time constants as shown in Table 2 for GaAs and InP. Fundamental frequency limits of 100 GHz for GaAs and 200 GHz for InP TEDs are estimated from these effective transfer time constants. In subsequent sections, some solutions that help reduce the dead-space region or extend the useful frequency range close to or even beyond these fundamental frequency limits are presented and discussed.

FABRICATION TECHNOLOGIES

TEDs are characterized by low-to-medium dc-to-RF conversion efficiencies ranging from approximately more than 15% down to less than 1%. As a consequence, most of the dc input power P_{DC}, i.e., $P_{DC} - P_{RF}$ needs to be dissipated as heat in the device. In most cases, one of the metal contacts near the active region of the device also acts as the heat sink; therefore, TEDs for millimeter-wave frequencies generally are mesa-type devices. Additionally, operation at these frequencies requires thin devices to reduce losses in the substrate resulting from the skin effect. The integrated heat sink technology is the most widespread for devices at millimeter-wave frequencies. To reduce losses in the substrate, most of it needs to be removed during fabrication.

In early fabrication technologies, vapor-phase epitaxy provided the layer structures. As a first step in processing, a few small holes across the sample were etched through the epitaxial layers down into the substrate. An appropriate depth of the holes was chosen to gauge the thickness during substrate removal. The advent of more advanced growth techniques, such as MBE, MOMBE, MOCVD, and CBE, allows the incorporation of a lattice-matched, stop-etch layer between the substrate and the epitaxial layers of the device. This way, the substrate is completely removed, and precise control of the mesa height and, consequently, the device diameter is achieved. Fabrication technologies for substrateless devices on integral heat sinks or on diamond heat sinks for better heat removal have been developed and described in the literature. Selective etching technologies in the GaAs and InP material systems (16–18) employ as etch-stop layers lattice matched $Ga_xAl_{1-x}As$ ($x < 0.4$), and $In_{0.53}Ga_{0.47}As$ layers, respectively. Improved yield, reproducibility, and performance characterize these substrateless devices.

Figure 10 summarizes the basic steps of these fabrication technologies. The batch fabrication of InP TEDs on integral heat sinks serves as an example (16). In the first step, the metalization for the n ohmic contact (Ni/Ge/AuTi/Au) is evaporated or sputtered onto the surface. A thick gold layer is then electroplated onto this metalization to form the integral heat sink. The sample is mounted on a carrier to provide additional mechanical support and protect the heat sink during the subsequent processing steps. The substrate is removed in a selective etchant of diluted HCl (16), which does not attack the $In_{0.53}Ga_{0.47}As$ etch-stop layer. Good ohmic contacts can be formed on InP or, with lower specific contact resistance ρ_c, on $In_{0.53}Ga_{0.47}As$. Therefore, this $In_{0.53}Ga_{0.47}As$ layer need not be removed, but may be etched away selectively in a standard solution of phosphoric or sulfuric acid, hydrogen peroxide, and water as indicated in Fig. 10. Such a solution does not attack InP. A photolithography step defines the openings on this InP

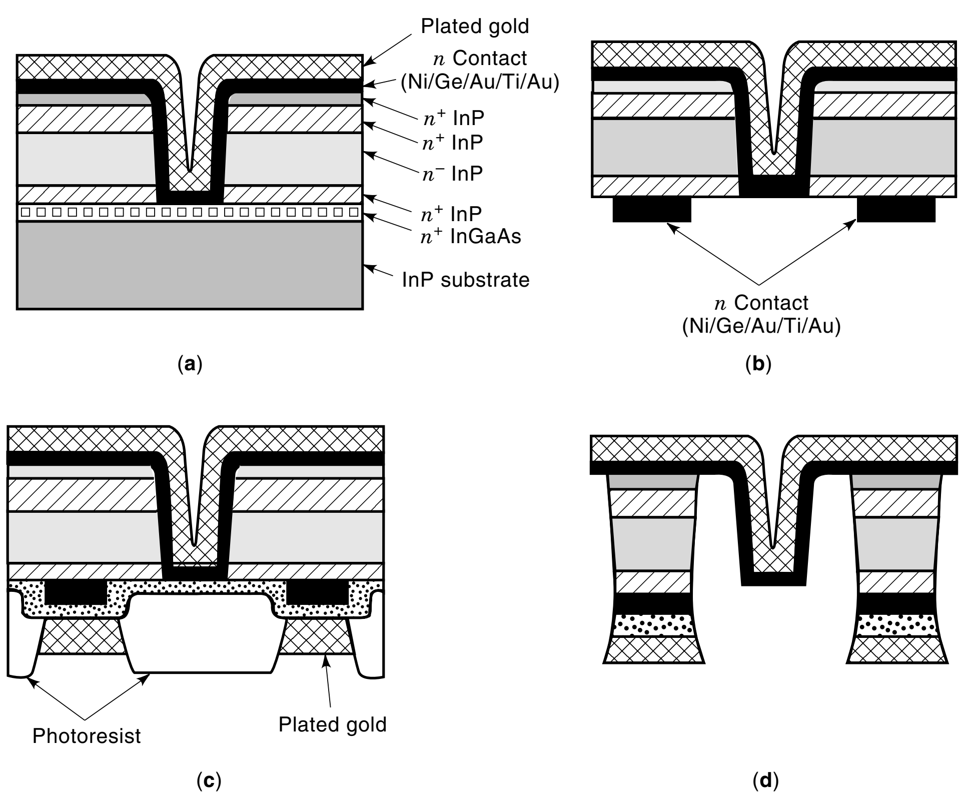

Figure 10. Steps in the fabrication of InP TEDs on integral heat sinks. (a) Island definition, n-ohmic evaporation, and gold plating of heat sink ($\approx$20 μm). (b) Substrate thinning, etch-stop layer removal, and second n-ohmic evaporation. (c) Gold plating of ohmic contacts. (d) Final devices after annealing and mesa etch. [After Kamoua et al. (16), with permission.]

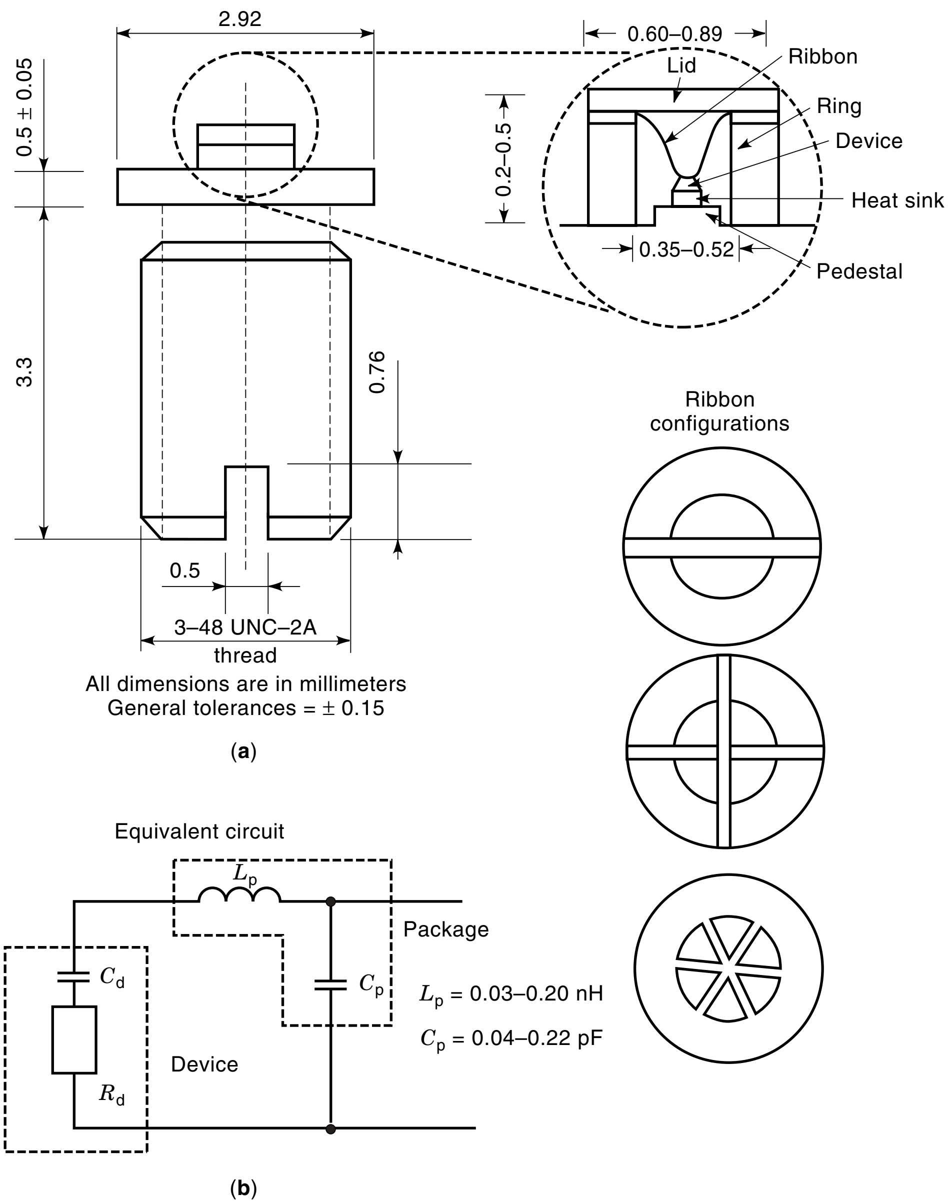

Figure 11. (a) Hermetically sealed package for millimeter-wave TEDs. (b) Equivalent circuit of the parasitic elements.

surface (or $In_{0.53}Ga_{0.47}As$ surface if left in place), where the metalization (Ni/Ge/Au/Ti/Au) for the other n-ohmic contacts on the second heavily n^+-doped layer is deposited. Excess metal outside the contacts is lifted off with the photoresist and, using another photolithography step, the contacts are selectively electroplated with several microns of gold to form a good bonding pad. The contact pad acts as a mask when the mesa of the diode is etched in a nonselective etch. After the sample has been removed from the carrier, the contacts are annealed, and the sample is diced into individual diodes. Diodes are then mounted in packages for appropriate RF circuits.

DEVICE PACKAGES, OSCILLATOR CIRCUITS, AND RF PERFORMANCE

Figure 11(a) shows a typical TED package. It consists of a gold-plated threaded copper puck (which can be screwed into the RF circuit), an alumina ring, and a top lid for a hermetic seal. The device is soldered or thermocompression-bonded onto a pedestal inside the ring, and gold straps are then thermocompression bonded to the device and the top metalization of the alumina ring. The height and diameter of the ring depend on the operating frequency as well as the device, and typical values are given in Fig. 11(a). This type of package is used up to frequencies of 94 GHz, and its parasitic elements can be approximated by lumped elements as illustrated in Fig. 11(b). Different ribbon configurations are chosen to minimize the influence of the parasitic inductance, which is the highest for just one gold strap across and the lowest for the “star” configuration. The useful frequency range of the package can be extended to 140 GHz and higher if the alumina ring is replaced by a quartz ring. However, new devices for frequencies above 100 GHz are still being developed, and, for research purposes, a low-parasitic open package with two or four standoffs at the highest millimeter- and up to submillimeter-wave frequencies is also often employed (18,19). The heat-flow resistance R_{th} from the active layer of the device to the package causes an average temperature increase ΔT in

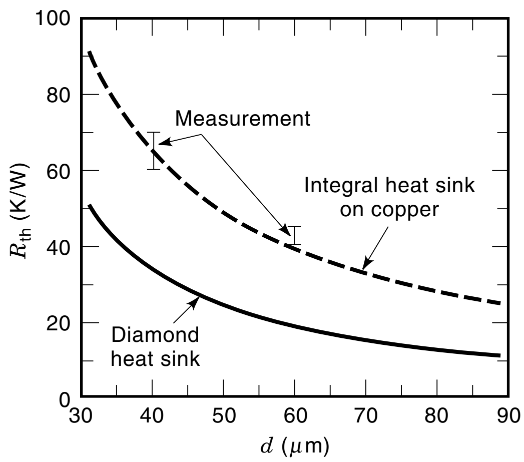

Figure 12. Estimated and measured (21–23) heat-flow resistances R_{th} of InP TEDs on integral heat sinks and estimated R_{th} of InP TEDs on diamond heat sinks against device diameter d; estimates are based on the spreading approximation (20).

the active layer

$$\Delta T = R_{th}(P_{DC} - P_{RF}) \tag{10}$$

Too high an active layer temperature degrades the RF performance as well as the device reliability and lifetime (11). A larger valley separation of 0.53 eV in InP than in GaAs (see Fig. 3) reduces the temperature dependence of the transfer mechanism as well as the temperature dependence of the effective transit velocity v_T (see Table 2). As a result, dc-to-RF conversion efficiencies and oscillation frequencies are generally less temperature dependent in InP Gunn devices. However, the higher threshold electric field of 10.5 kV cm^{-1} in InP (see Table 2) requires higher bias voltages than those applied at GaAs devices of the same length. Therefore, RF power levels are thermally limited at low microwave frequencies, where long active regions need to be used. As a further consequence, InP TEDs are more likely to benefit from reduced heat-flow resistances (11). Figure 12 compares the estimated (20) heat-flow resistances of W-band (75 to 110 GHz) and D-band (110 to 170 GHz) InP Gunn devices on integral and diamond heat sinks as well as some measured values for devices on integral heat sinks (21–23). Examples of how diamond heat sinks improve the RF performance of both GaAs and InP Gunn devices are provided in the section on device structures.

Many different circuit configurations for oscillators with TEDs have been investigated. At millimeter-wave frequencies, waveguide circuits are quite common. Although excellent results were reported from a few transferred-electron oscillators (TED) in microstrip circuits (10,11,24,25), the vast majority of the state-of-the-art-results was obtained in waveguide circuits. These results are summarized in Fig. 13 and include the performance of different device structures as illustrated in Fig. 7. Examples for the RF performance of individual device structures will be given in the subsequent section. An overview of typical configurations for waveguide circuits (26,27) is shown in Fig. 14. Examples of oscillator circuits using coaxial lines at microwave frequencies can be found in Ref. 1.

DEVICE STRUCTURES

Ohmic Cathode Contacts

TEDs with ohmic contacts on both heavily n-doped regions of the structure of Fig. 7(a) are the simplest structure, easy to fabricate, but characterized by low dc-to-RF efficiencies. These devices are typically operated in a full-height waveguide cavity with a resonant cap on top of the device package, and this configuration is illustrated in Fig. 14(e). Modifications of this configuration include the use of a reduced-height waveguide or a mechanism for adjusting the position of the resonant cap and the device package with respect to the bottom of the waveguide. Fundamental-mode operation of Gunn devices in a reduced-height post-coupled waveguide cavity was reported up to millimeter-wave frequencies, e.g., for a GaAs Gunn device at 84 GHz (28) and an InP Gunn device at 126 GHz (29). RF power levels (and corresponding dc-to-RF conversion efficiencies) of 420 mW (6%) at 35 GHz (19), 280 mW at 45 GHz (19), 150 mW at 60 GHz, and 110 mW (2.8%) at 70 GHz (30) were reported from flat-profile GaAs Gunn devices in the fundamental mode.

A sharp decline in the dc-to-RF conversion efficiencies of devices operating in the fundamental-mode presages the above frequency limits for GaAs or InP Gunn devices. However, this frequency limit can be extended by the extraction of higher harmonics from the inherently nonlinear Gunn device.

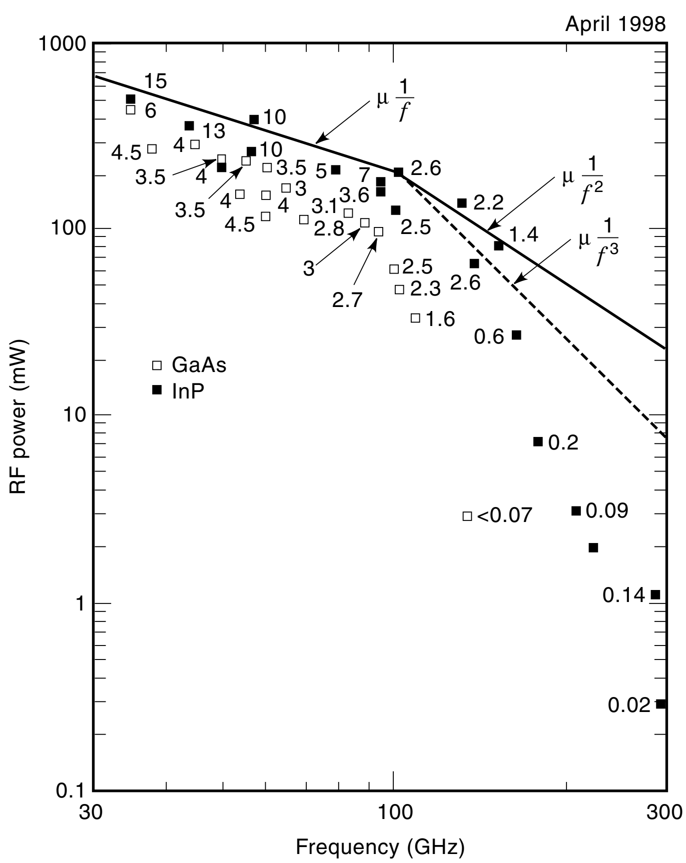

Figure 13. State-of-the-art RF power levels from TEDs under CW operation in the frequency range of 30 GHz to 300 GHz. Numbers next to the symbols denote dc-to-RF conversion efficiencies, expressed in percent.

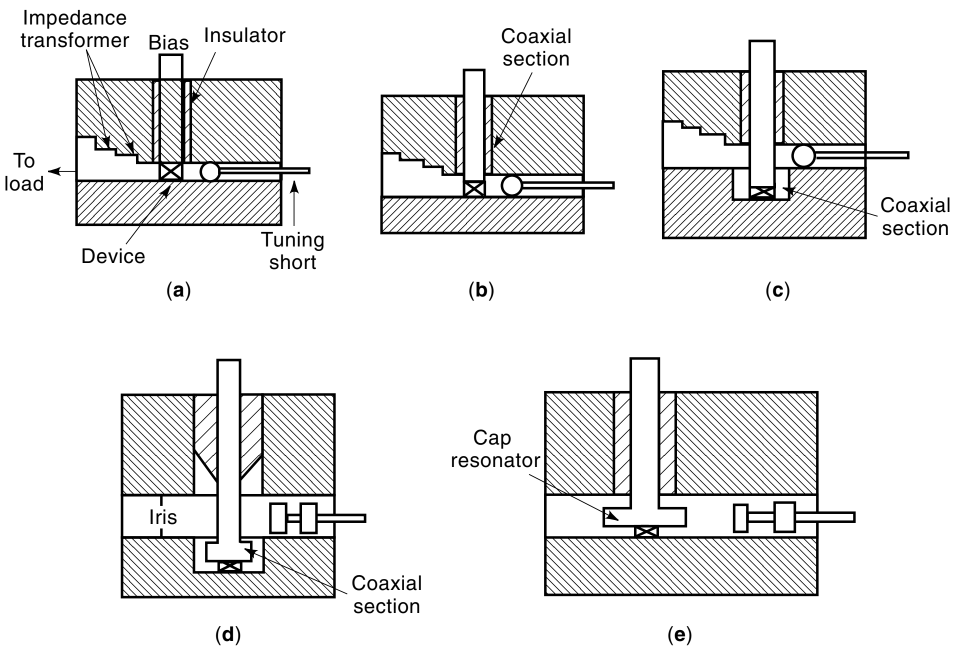

Figure 14. Examples of waveguide circuits for TED oscillators. [After Kuno (26), with permission.]

Second-harmonic power extraction has been proven most successful in a slightly modified version of a resonant-cap, full-height waveguide cavity. The size of the waveguide is appropriate for the second-harmonic frequency, but impedes propagation at the fundamental frequency. If in such a circuit the fringe capacitance of the cap and the device capacitance together resonate with the inductance of the bias post [see Fig. 14(e)] at half the output frequency, this signal cannot propagate, and the device is mainly reactively terminated at the fundamental frequency. This reactive termination causes a large voltage swing in the device and, as a result, strong nonlinear operation. A cap of appropriate size together with the coaxial post provides impedance matching into the waveguide at the second-harmonic frequency, and a waveguide back short at one side of the cavity provides power tuning. The resonant circuit at the fundamental frequency is decoupled from the load, which corresponds to typically higher Q values than those in fundamental-mode operation. As a result, reduced frequency pulling with load changes or improved frequency stability may be observed. However, more complicated circuits with precise mechanical dimensions are necessary if wide-range frequency tuning is to be implemented. As an example for second-harmonic power extraction, RF power levels (and dc-to-RF conversion efficiencies) of 123 mW (3.1%) at 83 GHz and 96 mW (2.7%) at 94 GHz were measured with GaAs Gunn devices (30).

The advantages of InP can be seen clearly at millimeter-wave frequencies with short active regions where lower inertial energy time constants lead to a higher fundamental frequency limit of approximately 200 GHz. RF power levels (and corresponding dc-to-RF conversion efficiencies) of 200 mW (5%) at 80 GHz and 150 mW (3.5%) at 94 GHz (22) in the fundamental mode as well as 7 mW at 180 GHz and 3.2 mW at 206 GHz (31) in a second-harmonic mode were reported from similar InP Gunn devices on integral heat sinks.

Power stability against package temperature typically ranges from −0.02 dB/°C to −0.06 dB/°C as quoted by various manufacturers for commercially available GaAs Gunn devices (see also Ref. 11). Conversely, values of around −0.013 dB/°C (11) or as low as −0.005 dB/°C (21,22) were reported from InP Gunn devices.

Current-Limiting Cathode Contacts

A partially annealed ohmic contact significantly reduces the typical Schottky barrier height of metals on the semiconductors GaAs and InP (0.6 eV to 0.9 eV), but still leaves a small barrier (<200 meV). If such a contact is formed on the cathode side of the two-zone structure [see Fig. 7(b)] and is reverse biased, this barrier causes a high-field region at the cathode contact of the device under bias. Electrons injected over this barrier into the active region have a higher energy and, under this high electric field, transfer faster into the upper valleys. This faster transfer reduces the dead space. The shallow Schottky barrier also limits the current flow into the active region at the cathode. Thermionic emission and thermionic-field emission contribute to the current flow, and, in this case, the current density J_c as a function of the voltage V_c across the barrier can be approximated by

$$J_c(V_c) = J_r\left\{\exp\left(-\frac{qV_c}{nkT}\right) - \exp\left[\frac{(1-n)qV_c}{kT}\right]\right\} \tag{11}$$

In Eq. (11), the saturation current $J_r = A^*T^2\exp(-q\phi_{Bn}/kT)$ and k, T, r, A^*, $q\phi_{Bn}$ denotes the Boltzmann constant, absolute temperature, ideality factor, effective Richardson constant, and effective barrier height on n-type materials, respectively (1). Current limiting as a boundary condition at the cathode causes the electrons in the active region of the device to approximate the current valley condition (15,32) for a saturated electron velocity v_s and a doping concentration n_D,

$$\overline{J(t)} = J_0 = n_D q v_s \tag{12}$$

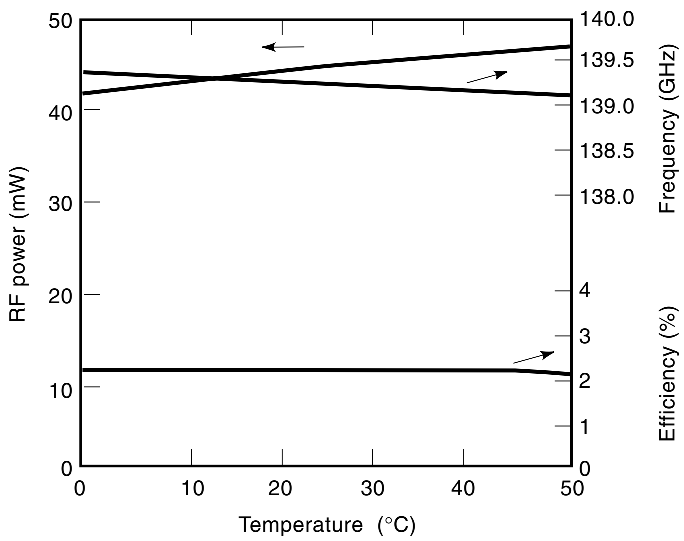

Figure 15. Measured RF performance of a D-band InP Gunn device as a function of the ambient temperature. [After Crowley et al. (23), with permission.]

with large space-charge waves superimposed on an almost constant electric field throughout the active region (15). This mode of operation yields high RF power levels in the fundamental mode as well as a second-harmonic mode. Corresponding dc-to-RF conversion efficiencies are typically the highest reported to date. RF power levels (and dc-to-RF conversion efficiencies) of more than 500 mW (15%) at 35 GHz, more than 350 mW (13%) at 44 GHz and 380 mW (10.6%) at 57 GHz (19,33) in the fundamental mode as well as 175 mW (7%) at 94 GHz and 65 mW (2.6%) at 138 GHz (23,34) in a second-harmonic mode were achieved using this technology. These devices are on integral heat sinks, and still higher RF power levels are expected from devices on diamond heat sinks. Devices on integral heat sinks with high RF power levels are also commercially available.

Equation (11) expresses the strong temperature dependence that is inherent in the current flow through a shallow Schottky barrier in the reverse direction (1). However, the high-efficiency mode reduces dc input requirements and provides higher impedance levels. As a consequence, larger device diameters can be used, which have lower heat-flow resistances (see Fig. 12). In turn, lower heat-flow resistances R_{th} entail lower active-layer temperatures [see Eq. (10)]. The typical temperature increase remains below 100 K at maximum RF output power (23,33), and low operating active-layer temperatures ensure reliability and excellent temperature stability over wide temperature ranges of −30°C to +70°C for devices at 56 GHz (33) and 94 GHz (33,34) as well as of 0°C to 50°C for devices at 140 GHz (23). The temperature-dependent performance of a D-band InP Gunn device in Fig. 15 serves as an example.

Graded Active Region

A doping profile with a lower doping concentration N_D at the cathode and a linear grading toward a higher N_D at the anode decreases the peak electric field near the anode to a large extent and increases the electric field near the cathode (16). Both effects are beneficial to the device operation, and they enhance the dc-to-RF conversion efficiency as well as the RF output power of the device. A lower electric field near the anode reduces the power dissipation in this region and also allows higher bias voltages without the onset of impact ionization and avalanche breakdown. A higher electric field near the cathode causes a larger fraction of the electrons to transfer to the upper valleys over a shorter distance, which is equivalent to a shorter dead-space region. This is illustrated in Fig. 16, which compares domain formation in a flat-profile [Fig. 15(a)] and a graded-profile [Fig. 15(b)] TED structure, both with a 1.0-μm-long active region. Accumulation domains form in the flat-profile structure, whereas dipole domains form in the graded-profile structure. A higher fraction of electrons in the upper valleys slightly lowers the average electron velocity throughout the active region; as a consequence, the graded-profile structure operates at lower current densities compared to a flat-profile structure of a similar doping concentration. As a matter of fact, a lower average electron velocity and shorter dead space may somewhat decrease the optimum operating frequency for the same device length. However, more efficient device operation extends the upper frequency limit and allows shorter active regions. Structures with graded doping profiles were investigated in both InP and GaAs material systems.

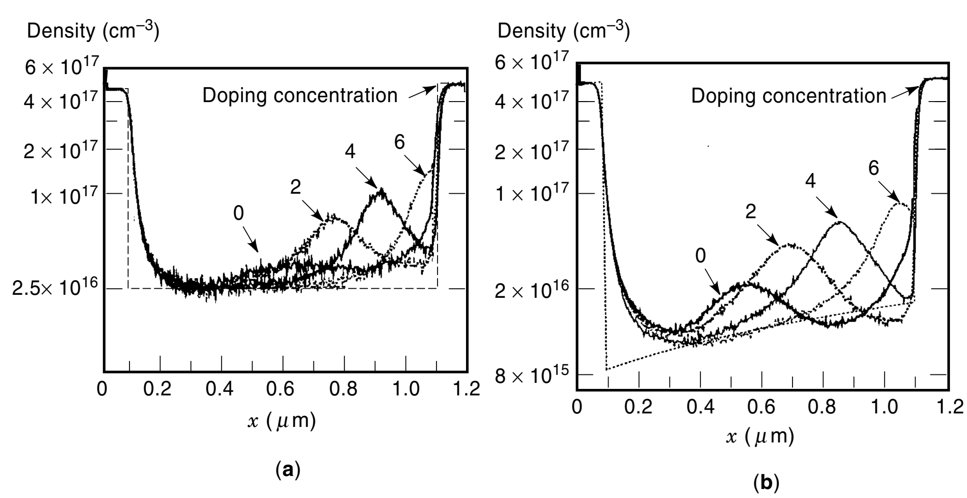

Figure 16. Evolution of electron density as a function of position x (active region from 0.1 μm to 1.1 μm) for a flat-profile (a) and graded-profile (b) TED structure at f = 130 GHz and $\omega t = n\pi/4$, n = 0, 2, 4, 6, during one RF cycle.

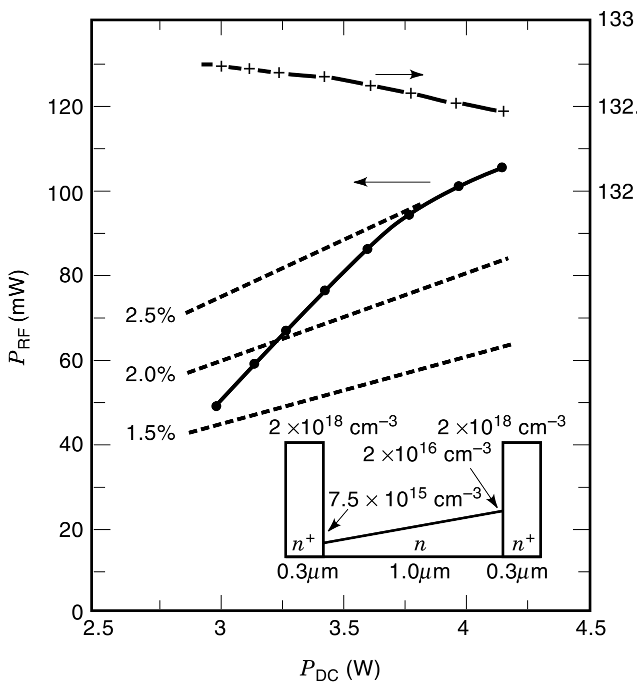

Figure 17. Bias-dependent RF characteristics of a D-band InP Gunn device (●, output power, +, oscillation frequency, ---, lines of constant efficiency). Inset: Nominal doping profile. [After Eisele and Haddad (29), with permission.]

RF power levels (and dc-to-RF conversion efficiencies) of 345 mW (6.8%) at 31.2 GHz and 325 mW (6.6%) at 34.9 GHz from devices on integral heat sinks (35) and 116 mW (4.5%) from devices on diamond heat sinks (36) around 60 GHz were achieved in the GaAs material system. The devices on diamond heat sinks showed operating active-layer temperatures below 150°C and fundamental-mode operation up to 84 GHz (33 mW and 1.7%) (36). Devices from InP material with the properly designed (16) graded doping profile of Fig. 16(b) yielded the highest RF power levels reported for any Gunn device to date. Fundamental-mode operation was demonstrated up to 165 GHz, and RF power levels that exceeded 200 mW at 103 GHz, 130 mW around 132 GHz, 80 mW at 152 GHz, and 25 mW at 163 GHz (37) were obtained from devices on diamond heat sinks (29). As an example, dc-to-RF conversion efficiencies exceeded 2.3% between 102 GHz and 132 GHz (38). RF power levels exceeding 2 mW around 223 GHz (39) and exceeding 1 mW at 280 GHz (37) as well as 315 GHz were measured in a second-harmonic mode. As illustrated in Fig. 17, the InP Gunn devices on diamond heat sinks allow single-mode operation over a wide range of dc input power levels. Excellent tuning behavior was also observed, which can be expected from operation in the fundamental mode. This tuning behavior over a range of more than 4.5 GHz is shown in Fig. 18 for the device of Fig. 17 near maximum dc bias. The oscillation frequency changes almost linearly with the position of the back short, which is the only tuning element in this full-height waveguide resonant-cap cavity [see Fig. 14(e) for a schematic]. Improved dc-to-RF conversion efficiencies reduce the dc input power requirements for the same RF power levels, and, similar to devices with current-limiting cathode contacts, lower the operating active-layer temperatures, in particular on diamond heat sinks (29,36).

Injection Over a Homo- or Heterojunction Barrier

Injection of hot electrons over a barrier reduces the dead space in the active region. Several concepts (e.g., planar-doped barrier, camel cathode, and heterojunction barriers) have been investigated in GaAs to improve efficiency, but also to eliminate cold-start problems in GaAs Gunn devices. Injection over a heterojunction barrier has been proven the most successful and was experimentally investigated in the AlGaAs/GaAs system with improved efficiencies and upper frequency limits (28,40). Figure 19 shows the band diagrams of isotype heterojunctions in the lattice-matched $GaAs/Al_xGa_{1-x}As$ and $InP/In_xGa_{1-x}As_yP_{1-y}$ material systems. In both material systems, layers can be grown lattice-matched over a wide composition range, and thus bandgap or conduction band offset can be tailored suitably.

Linear composition grading from the GaAs to the wide bandgap AlGaAs eliminates the first barrier, and the doping spike as shown in Fig. 7(d) at the beginning of the active region (GaAs) reduces or eliminates the notch at the interface from the AlGaAs layer to the GaAs region. At the proper bias level, “hot” electrons are now ballistically launched into the active region from an approximately 200 meV high step in the conduction band. The optimization of such a design requires advanced simulation schemes, such as ensemble Monte Carlo techniques. Using a reduced-height post-coupled waveguide cavity [see Fig. 14(b) for a schematic] for the oscillator, an RF output power of 71 mW with a corresponding dc-to-RF conversion efficiency of 2.8% was measured in the fundamental mode at 77.6 GHz. Low-noise operation of such a Gunn device was achieved at least up to 84 GHz (28). As a characteristic of fundamental-mode operation (29), a wide tuning bandwidth of more than 6 GHz was observed by simply adjusting the position of the back short (28).

In contrast to the GaAs/AlGaAs material system, lattice-matched InGaAsP has a smaller band gap than InP as illustrated in Fig. 19. Therefore, electrons cannot be ballistically launched into the active region. However, a wide composition

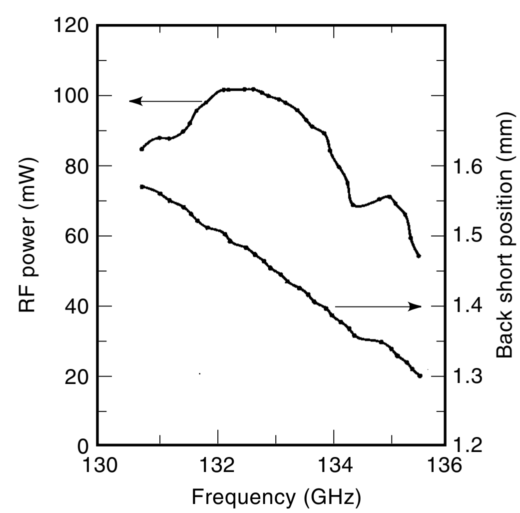

Figure 18. Mechanical tuning characteristic for the D-band InP Gunn device of Fig. 17 close to maximum applied bias.

range in the InGaAsP material system can be lattice-matched to InP. This wide composition range allows a wide range in the bandgap and conduction-band offset to be implemented. As a consequence, the proper current-limiting injection at the cathode can be designed. Theoretical investigations predict a significant improvement in dc-to-RF conversion efficiencies at W-band and D-band frequencies (32,41) while preserving the higher-frequency limit of InP compared to GaAs.

In summary, different schemes for "accelerating" electrons and transferring them faster into the upper valleys can be incorporated in a device design. Shorter transfer times reduce the dead space, improve the dc-to-RF conversion efficiency, and allow for a shorter active region to achieve a higher operating frequency. However, a reduced dead space effectively increases the transit time and actually lowers the optimum operating frequency for an active region of the same length. Finite transfer times still impose a physical upper frequency limit. Additionally, if electrons gain too much energy and/or the active region is too short, the long energy relaxation time prevents the electrons from losing enough energy to transfer back to the lower valley. No domains can form in such a structure, the dynamic resistance between the two terminals remains positive for all frequencies, and no RF power is generated.

NOISE

The noise in the output spectrum of an oscillator consists of fluctuations in amplitude (AM noise) and oscillation frequency (FM noise). However, FM noise generally dominates in Gunn devices and can be described as effective frequency modulation Δf_{rms} versus frequency f_m off the oscillation frequency f_o. It corresponds to the noise-to-carrier ratio $N/C|_{FM}$ as, for example, seen on a spectrum analyzer

$$\left.\frac{N}{C}\right|_{FM} = \frac{\Delta f_{rms}^2}{2f_m^2} \tag{13}$$

To compare the noise performance of different oscillators including those with other two-terminal devices on a more equitable basis, the FM noise measure M (42) is more appropriate:

$$M = \frac{\Delta f_{rms}^2 Q^2}{f_o^2 k T_0 B} P_{RF} \tag{14}$$

where T_0 is the absolute temperature and B is the bandwidth. The loaded Q factor of the oscillator circuit is determined in a waveguide setup as illustrated in Fig. 20(a). The sweep oscillator injects a signal at the power level P_i into the oscillator-under-test (OUT), and the maximum continuous frequency range Δf_s over which the OUT remains injection-locked with the sweep oscillator is determined (42):

$$Q = \frac{2f_o}{\Delta f_s}\sqrt{\frac{P_i}{P_{RF}}} \tag{15}$$

An alternative is also shown in Fig. 20(b). The signal from the OUT is reflected at a tunable low-loss back short and injected back as P_i through the coupler into the OUT. If the position of the back short is moved by more than half of the guide wavelength λ_g, the oscillation frequency continuously changes from a lower to an upper limit. This maximum tuning range (i.e., the self-injection locking range) is now Δf_s in Eq. (15).

Thermal noise of electrons is the dominant effect in Gunn devices. If a TED is designed (using subcritical $N_D l < 1 \times 10^{12}$ cm^{-2}) for and operated in the amplifier mode (1), the small-signal noise measure M approaches the asymptotic limit M_0:

$$M_0 = \frac{qD}{k|\overline{\mu}_d|T_0} \tag{16}$$

where the ratio of the diffusion coefficient D and the differential mobility $|\overline{\mu}_d|$ is the crucial factor. InP shows an advantage of 142/72 (~3 dB, see Table 2) over GaAs. If an equivalent differential mobility μ_{eff} is introduced for the oscillator mode (critical $N_D l > 1 \times 10^{12}$ cm^{-2}) with the conductance per unit area G_D,

$$\mu_{eff} = \frac{|G_D|}{qN_D} \tag{17}$$

the large-signal noise measure M can be defined as

$$M = \frac{qD}{k\mu_{eff}T_0} \tag{18}$$

The noise performance of Gunn devices near the carrier is dominated by flicker noise components with typical corner

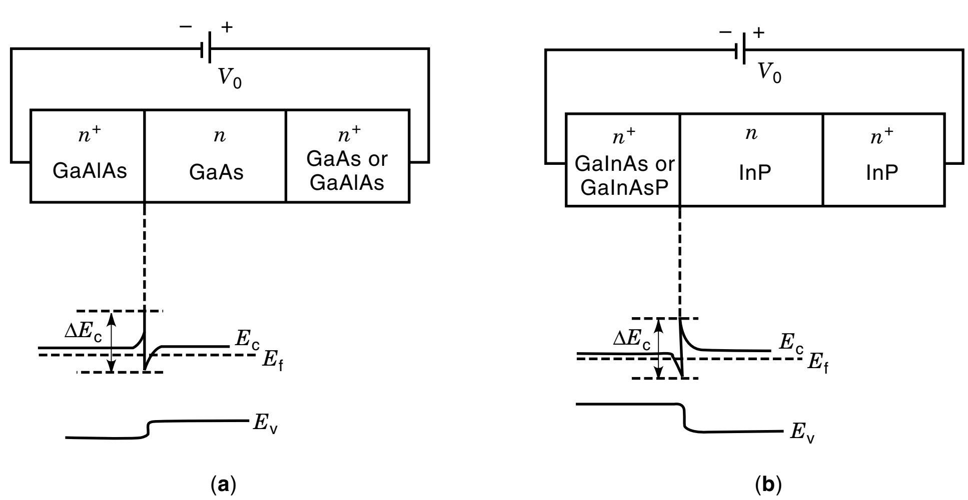

Figure 19. Band diagram of isotype heterojunctions in GaAs/AlGaAs and InP/InGaAsP at zero bias. [After Friscourt et al. (32), with permission.]

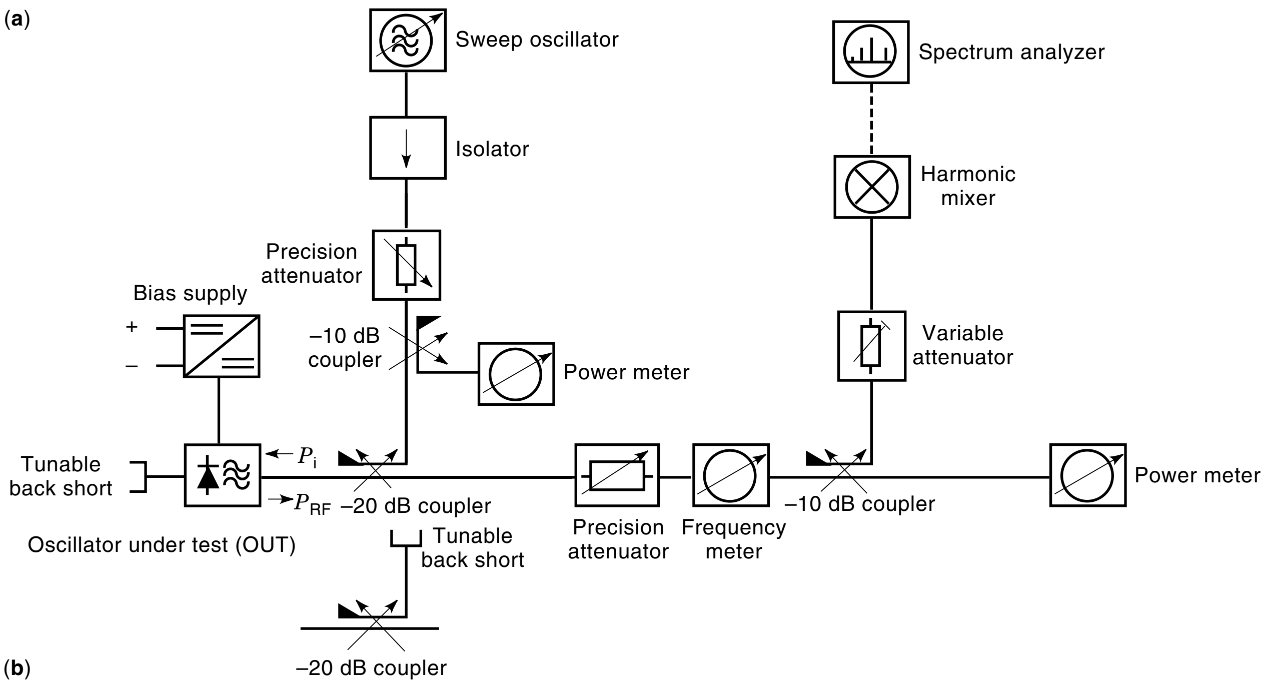

Figure 20. Waveguide test setup to determine the injection locking range Δf_s and Q factor of a transferred-electron oscillator. (a) Using injection locking with a sweep oscillator, (b) using self-injection locking.

frequencies in the range of 100 kHz to 1 MHz. As predicted by Eq. (13), the phase noise decreases −20 dB per decade at higher off-carrier frequencies. Table 3 summarizes typical results from GaAs and InP Gunn devices (24,28,29,43).

Although Eq. (18) predicts lower M for oscillators with InP Gunn devices, experimental results indicate little difference between the two. Figure 21 (39) compares the FM noise measure M of Gunn devices with that of other two-terminal devices in the frequency range of 75 GHz to 155 GHz. This figure highlights the low-noise characteristics of TEDs, where the large-signal FM noise measure of both GaAs and InP Gunn devices typically remains below 25 dB (11,24,29,43,44). Some InP devices with current-limiting contacts show excess flicker-noise components near the carrier frequency. Oscillators with Gunn devices in a second-harmonic mode yield lower values for the phase noise, but they yield similar values for the noise measure because much higher Q values are achieved in a circuit without a resistive load at the fundamental frequency.

FUTURE TRENDS

Fundamental-mode operation up to 165 GHz was demonstrated with InP Gunn devices. Therefore, InP or InP with heterojunction barriers are promising material systems not only for device structures that exhibit improved performance in the fundamental mode at frequencies around or above 100

Table 3. Phase Noise of Free-Running Oscillators Using GaAs or InP Millimeter-Wave Gunn Devices

Material System	Phase Noise (dBc/Hz)	Off-Carrier Frequency (kHz)	Oscillation Frequency (GHz)	RF Output Power (mW)	Reference
GaAs	<−80[a]	100	77	>40[a]	28
GaAs	−70	100	80	55	24
GaAs	−100	1000	80	55	24
GaAs	−120	10000	80	55	24
GaAs	−80	100	94	10	43
GaAs	−105	1000	94	10	43
InP	−75	100	94	20	43
InP	−100	1000	94	20	43
InP	<−110	500	103	180	[b]
InP	<−108	500	132	120	29
InP	<−103	500	151	58	29

[a] Reported as typical value; corresponding RF output power not mentioned.
[b] H. Eisele, 1997 (unpublished).

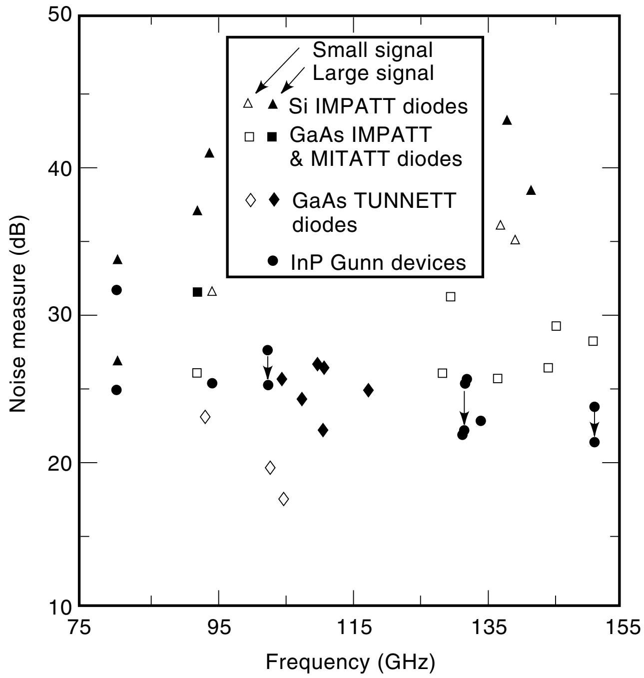

Figure 21. Comparison of the FM noise measure M in free-running oscillators with different two-terminal devices at millimeter-wave frequencies from 75 GHz to 155 GHz. [After Eisele and Haddad (39), with permission.]

GHz, but also for other device structures that generate significant RF power levels up to 320 GHz in a second-harmonic mode. In all these devices, proper heat management is one of the important factors, and the employment of the appropriate diamond heat sink technologies is mandatory for maximum RF output power as well as reliable long-term operation. Power-combining techniques (27,45) can be employed to increase the available RF power levels. As examples, four InP Gunn devices in a power-combiner circuit delivered an RF power of 260 mW to the load in CW operation at 98.6 GHz (11,46) and two devices on diamond heat sinks delivered more than 300 mW at 103 GHz (38) or more than 125 mW at 152 GHz (39).

Wide-bandgap materials such as GaN and AlGaN hold great promise for high-power Gunn devices. Favorable material parameters, for example, are higher critical electric fields for breakdown, higher thermal conductivities, higher permissible operating temperatures, and expected higher carrier drift velocities. However, high-threshold electric fields ϵ_{Th} may result in thermal limitations of the RF performance. Furthermore, major improvements in material quality or availability and in fabrication technologies are needed before devices for system applications can be developed.

Waveguide circuits are, in general, rugged, can dissipate heat easily, and offer high Q values. Therefore, they are the preferred circuits to obtain the maximum RF output power. However, they are bulky and in most cases must be machined, assembled, and tested individually, which prohibits low-cost mass production. Therefore, high-volume production for system applications such as wireless communication (high-speed data transmission) or collision avoidance in automobiles must be based on quite different approaches. Both hybrid and monolithic integration were attempted with Gunn devices. Hybrid microstrip-line oscillators with InP Gunn devices exhibited excellent performance. RF power levels (with corresponding dc-to-RF conversion efficiencies) of 52 mW (3.5%) at 94 GHz (25), but also 40 mW (1.4%) at 81 GHz (11,24), and >200 mW (>7.5%) around 35.5 GHz (10,34) were measured and are considered comparable to values from similar Gunn devices in waveguide circuits. The thermal conductivity of the semiconductor materials InP and GaAs is rather low (0.68 $W \cdot cm^{-1} \cdot K^{-1}$ and 0.46 $W \cdot cm^{-1} \cdot K^{-1}$, respectively) when compared to metals or diamond (20 $W \cdot cm^{-1} \cdot K^{-1}$ at room temperature). Therefore, fully monolithic integration of low-efficiency Gunn devices at millimeter-wave frequencies encounters severe thermal limitations. A summary of reports on integration of Gunn devices at frequencies up to approximately 68 GHz can be found elsewhere (27).

BIBLIOGRAPHY

1. S. M. Sze, *Physics of Semiconductor Devices,* 2nd ed., New York: Wiley, 1981.
2. U. V. Bhapkar and M. S. Shur, Monte Carlo calculation of velocity-field characteristics of wurtzite GaN, *J. Appl. Phys.,* **82** (4): 1649–1655, 1997.
3. S. Krishnamurthy et al., Bandstructure effect on high-field transport in GaN and GaAlN, *Appl. Phys. Lett.,* **71** (14): 1999–2001, 1997.
4. B. K. Ridley and T. B. Watkins, The possibility of negative resistance effects in semiconductors, *Proc. Phys. Soc. London,* **78**: 293–304, 1961.
5. C. Hilsum, Transferred electron amplifiers and oscillators, *Proc. Inst. Radio Eng.,* **50**: 185–189, 1962.
6. J. B. Gunn, Microwave oscillation of current in III–V semiconductors, *Solid-State Commun.,* **1**: 88–91, 1963.
7. J. B. Gunn, Instabilities of current in III–V semiconductors, *IBM J. Res. Develop.,* **8**: 141–159, 1964.
8. H. Kroemer, Theory of the Gunn effect, *Proc. IEEE,* **52**: 1736, 1964.
9. L. Wandinger, mm-wave InP Gunn devices: Status and trends, *Microw. J.,* **24** (3): 71–78, 1981.
10. B. Fank et al., Basics and recent applications of high-efficiency millimeter wave InP Gunn diodes, *Proc. 1st Int. Conf. Indium Phosphide Related Mater. Advanced Electron. Opt. Devices,* Norman, Oklahoma, SPIE, Vol. 1144, 1989, pp. 534–546.
11. I. G. Eddison, Indium Phosphide and Gallium Arsenide Transferred-Electron Devices, *Infrared and Millimeter Waves,* vol. 11, *Millimeter Components and Techniques, part III,* New York: Academic Press, 1984, pp. 1–59.
12. J. A. Copeland, LSA oscillator-diode theory, *J. Appl. Phys.,* **38**: 3096–3101, 1967.
13. P. N. Butcher, Theory of stable domain propagation in the Gunn effect, *Phys. Lett.,* **19**: 546–547, 1965.
14. J. F. Caldwell and F. E. Rosztoczy, Gallium arsenide Gunn diodes for millimeter-wave and microwave frequencies, *Proc. 4th Int. Symp. GaAs Related Compounds,* Denver, Colorado, 1972.
15. P. A. Rolland et al., Millimeter wave solid-state power sources, *Proc. Int. Workshop Millimeter Waves,* Rome, 1986, pp. 125–177.
16. R. Kamoua, H. Eisele, and G. I. Haddad, D-band (110–170 GHz) InP Gunn devices, *Solid-State Electron.,* **36**: 1547–1555, 1993.
17. H. Eisele, Selective etching technology for 94-GHz GaAs IMPATT diodes on diamond heat sinks, *Solid-State Electron.,* **32**: 253–257, 1989.

18. H. Eisele and G. I. Haddad, D-band InP Gunn devices with second-harmonic power extraction up to 290 GHz, *Electron. Lett.,* **30**: 1950–1951, 1994.
19. Y. E. Ma, Millimeter-wave active solid-state devices, *Millimeter Wave Technology III,* SPIE vol. 544, 1985, pp. 95–102.
20. L. W. Holway and M. G. Adlerstein, Approximate formulas for the thermal resistance of IMPATT diodes compared with computer calculations, *IEEE Trans. Electron Devices,* **ED-24**: 156–159, 1977.
21. M. A. di Forte-Poisson et al., High-power high-efficiency LP-MOCVD InP Gunn diodes for 94 GHz, *Electron Lett.,* **20**: 1061–1062, 1984.
22. M. A. di Forte-Poisson et al., LP-MOCVD InP Gunn devices developed for 94 GHz millimeter range operation, *Proc. 1st Int. Conf. Indium Phosphide Related Mater. Advanced Electron. Opt. Devices,* Norman, Oklahoma, SPIE, vol. 1144, 1989, pp. 551–560.
23. J. D. Crowley et al., 140 GHz indium phosphide Gunn diode, *Electron. Lett.,* **30**: 499–500, 1994.
24. D. C. Smith, T. J. Simmons, and M. R. B. Jones, A comparison of the performance of millimeter-wave semiconductor oscillator devices and circuits, *Dig. 1983 IEEE MTT-S Int. Microw. Symp.,* 1983, Boston, pp. 127–129.
25. C. Kim et al., Millimeter-wave tunable microstrip InP Gunn oscillators, *Microw. J.,* **32** (4): 91–102, 1989.
26. H. J. Kuno, IMPATT Devices for Generation of Millimeter Waves, in K. Button, (ed.), *Infrared and Millimeter Waves,* New York: Academic Press, 1979, chap. 2.
27. K. Chang, *Handbook of Microwave and Optical Components,* vol. 2, New York: Wiley, 1990.
28. I. Dale, J. R. P. Stephens, and J. Bird, Fundamental-mode graded-gap Gunn diode operation at 77 and 84 GHz, *Proc. Microwaves 94,* London, 1994, pp. 248–251.
29. H. Eisele and G. I. Haddad, High-performance InP Gunn devices for fundamental-mode operation in D-band (110–170 GHz), *IEEE Microw. Guided Wave Lett.,* **MGWL-5**: 385–387, 1995.
30. S. J. J. Teng and R. E. Goldwasser, High-performance second-harmonic operation W-band Gunn devices, *IEEE Electron Device Lett.,* **EDL-10**: 1989, pp. 412–414.
31. A. Rydberg, High efficiency and output power from second- and third-harmonic millimeter-wave InP-TED oscillators at frequencies above 170 GHz, *IEEE Electron Device Lett.,* **EDL-11**: 439–441, 1990.
32. M-R. Friscourt, P-A. Rolland, and M. Pernisek, Heterojunction cathode contact transferred-electron oscillators, *IEEE Electron Device Lett.,* **EDL-6**: 497–499, 1985.
33. B. Fank, J. Crowley, and C. Hang, InP Gunn diode sources, *Millimeter Wave Technology III,* SPIE, vol. 544, 1985, pp. 22–28.
34. J. D. Crowley et al., InP Gunn diodes serve millimeter-wave applications, *Microw. RF,* **33** (3): 143–146, 1994.
35. J. Ondria and R. L. Ross, Improved performance of fundamental and second-harmonic MMW oscillators through active doping concentration contouring, *1987 IEEE MTT-S Dig.,* 977–980, 1987.
36. K. Akamatsu et al., High-efficiency millimeter-wave GaAs Gunn diodes operating in the fundamental mode, *Dig. 19th Int. Conf. Infrared Millimeter Waves,* Sendai, Japan, 1994, pp. 89–90.
37. H. Eisele, GaAs TUNNETT diodes and InP Gunn devices for efficient second-harmonic power generation above 200 GHz, *Proc. 9th Int. Symp. Space Terahertz Technol.,* 1998, Pasadena, California, pp. 587–596.
38. H. Eisele and G. I. Haddad, Efficient power combining with D-band (110–170 GHz) InP Gunn devices in fundamental-mode operation, *IEEE Microw. Guided Wave Lett.,* **MGWL-8**: 24–26, 1998.
39. H. Eisele and G. I. Haddad, Two-terminal millimeter-wave sources, *IEEE Trans. Microw. Theory Tech.,* **MTT-46**: 739–746, 1998.
40. N. R. Couch et al., High-performance, graded AlGaAs injector, GaAs Gunn diodes at 94 GHz, *IEEE Electron Device Lett.,* **EDL-10**: 288–290, 1989.
41. R. Kamoua, Heterojunction D-Band (110 GHz–170 GHz) InP Gunn devices, *Solid-State Electron.,* **37**: 269–274, 1994.
42. K. Kurokawa, Noise in synchronized oscillators, *IEEE Trans. Microw. Theory Tech.,* **MTT-16**: 234–240, 1968.
43. C. Dalle, P. A. Rolland, and G. Lleti, Flat doping profile double-drift silicon IMPATT for reliable CW high-power high efficiency generation in the 94-GHz-window, *IEEE Trans. Electron Devices,* **ED-37**: 235–236, 1990.
44. D. M. Brookbanks, A M. Howard, and M. R. B. Jones, Si IMPATTs exhibit low noise at mm-waves, *Microw. RF,* **22** (2): 68–72, 1983.
45. K. Chang and C. Sun, Millimeter-wave power-combining techniques, *IEEE Trans. Microw. Theory Tech.,* **MTT-31**: 91–107, 1983.
46. J. J. Sowers, J. D. Crowley, and F. B. Fank, CW InP Gunn diode power combining at 90 GHz, *Dig. 1982 IEEE MTT-S Int. Microw. Symp.,* 1982, Dallas, TX, pp. 503–505.

Reading List

E. L. Holzman and R. S. Roberston, *Solid-State Microwave Power Oscillator Design,* Norwood, MA: Artech House, 1992.

S. M. Sze, *High-Speed Semiconductor Devices,* New York: Wiley, 1990.

S. M. Sze, *Modern Semiconductor Device Physics,* New York: Wiley, 1998.

K. S. Yngvesson, *Microwave Semiconductor Devices,* Norwell, MA: Kluwer, 1991.

HERIBERT EISELE
The University of Michigan